IET Power Electronics

*Research Article*

IET Journals
The Institution of Engineering and Technology

# Analysis of virtual synchronous generator control and its response based on transfer functions

ISSN 1755-4535
Received on 19th July 2018
Revised 14th May 2019
Accepted on 1st July 2019
E-First on 15th August 2019
doi: 10.1049/iet-pel.2018.5711
www.ietdl.org

*Junru Chen*[1] ✉, *Terence O'Donnell*[1]

[1]*University College Dublin, Dublin, Ireland*

✉ *E-mail: junru.chen.1@ucdconnect.ie*

**Abstract:** Virtual Synchronous Generator (VSG) control has been proposed as a means to control power electronics converter interfaced generation and storage which retains the dynamics of the conventional synchronous machine. This study provides a comprehensive, transfer function based, analysis of VGS control, which can be used as the basis for the design of VSG transient and steady-state performance. Based on a hardware validated, large signal model, a small signal model and associated transfer functions which describe the changes in real and reactive powers in response to changes in references and grid frequency disturbances. The derived transfer functions are used to obtain insight into the correct design of VSG controllers. The small signal models, transfer functions and associated analysis are validated by comparison with measured results on a scaled hardware system.

## 1 Introduction

The increase in penetration of power electronics connected renewable generation into the power system raises issues of power system stability. These inertia-less renewable energy sources decrease the total inertia of the network and potentially pose transient stability issues. In relation to this problem, Beck and Hesse proposed the Virtual Synchronous Machine (VSM) method in 2007 [1]. Its basic strategy is to control the Voltage Source Converter (VSC) to mimic the synchronous generator (SG) by implementing the swing equation in the control loop, thus emulating the inertia of a conventional generator. In this way, the DC side of the converter incorporating electrical energy storage mimics the virtual kinetic energy, [2] and the renewable energy source mimics the prime mover. Note both the terms and virtual SG (VSG) have since been used interchangeably in literature to denote this type of control approach, but for the sake of consistency in this work, we use only the VSG terminology.

Since the VSG concept had been proposed, different implementation methods have been designed [3]. Although some VSG control approaches have been applied to current source/grid feeding converters [4, 5], here the focus is on voltage source/grid forming converters which become necessary in the scenario of increased converter interfaced generation. The synchronisation of the grid forming VSG is analogous to the SG, relying on the filtered power synchronisation [6, 7], without the need for a phase-locked loop (PLL). The Synchronverter [8] was proposed with a self-synchronising method [9] to directly control the converter terminal voltage and this method has been further investigated in wind and PV systems [10–12]. The synchronverter is essentially a second-order SG emulation with the swing equation to determine voltage angle and a reactive power controller to determine voltage amplitude. Alternatively, the higher-order self-synchronised VSM topology, based on the outer voltage, inner current controlled converter, presented by D'Arco *et al.* [13–16], applies power-to-frequency control to achieve synchronisation and directly regulate the output voltage. This approach is one of the most general implementations [17–28] as it also features the inclusion of virtual impedance in the VSG which could help compensate the resistive line impedance. This method has also been investigated for wind generation [21, 22], electric vehicle systems [23] and other distributed energy resources [24–26]. These VSG controls were typically applied to storage systems or systems where the DC link voltage was regulated by the storage system. On the other hand, many renewable generation systems operate with a grid side converter the main function of which is to control the DC link. Considering the application of VSG control to these converters, it has been shown that the dynamics of the DC side capacitor are similar to those of the kinetic energy or inertia of the SG [29], and authors of [30, 31] proposed a VSG control method based on the DC link capacitor voltage dynamics. However, the VSG implementation of [13–16] has the strongest similarity with the conventional SG, with their control settings characterised by virtual inertia, damping and droop settings which can be directly analogous to the SG and giving similar performance if set identically [27]. For that reason, this work is most relevant to those VSG implementations.

An advantage of the VSM over the real synchronous machine is that the inertia and damping parameters are controller settings which can be easily varied (within the limits of ratings). Taking advantage of this, Alipoor *et al*. [32] suggested the use of varying inertia to rapidly reduce frequency oscillation after a contingency. Moreover, Li *et al*. [33] utilised a self-adaptive inertia and damping combination control on VSG to improve performance on both oscillation and settling time, although the mathematics relationship between VSG parameters and the oscillation reduction is missing in that paper. Although adaptive controls are not directly addressed in this work, the relationships developed can be used to give insight into adaptive control settings.

A solid mathematical basis for investigating the interaction between the VSG and the power system is vital in order to understand the possibilities which might arise from it in terms of enhancing power system performance. In this regard, D'Arco *et al.* [13–16] provide the overall small-signal modelling of VSG with the full Jacobian matrix. Based on this, Shuai *et al*. [34] applied Bifurcation Theory to synchronverter-based microgrid stability analysis. Although the Jacobian matrix could be used to analyse parametric sensitivity, the decoupled parametric effect on output power performance can be more clearly presented by transfer functions. In this respect, the authors of [35, 36] have provided a complex transfer function analysis with both VSG and VSC dynamics for the frequency to active power, while [37, 38] uses a simplified second-order transfer function for the frequency to active power considering virtual inertia and droop. Chen and O'Donnell [39] provided the transfer function for reference active power to actual power output and then analysed the VSG stability constraints. In addition, Wang *et al*. [40] used an angle to active power transfer function to analyse the influence of the virtual

resistance on active power. The benefit of transfer function analysis over state space analysis is its ability to provide more intuitive insight into the parametric effects on the response. While the state space approach, is appropriate for stability analysis in complex multi-input–multi-output systems it is not so easy to understand the direct effects of each parameter on the transient response. In other words, the transfer analysis put more emphasis on the device level analysis, although this analysis is limited to the single-input–single-output, while the state space approach is more appropriate for the system-level analysis. Therefore before studying the incorporation of the VSG in larger power systems, a more insightful analysis at the device level is required which adequately captures the VSG terminal characteristics, their interaction with the grid and the influence of the VSG settings on its characteristics. However, to the author's knowledge, there is no paper which provides the complete coupled analysis for voltage angle and magnitude and grid frequency to active and reactive power using transfer functions. Therefore the novel contributions of this paper are (i) to propose a VSG large-signal model, which is simplified compared with models in [13–16] and mainly focuses on the VSG parameters; (ii) to provide not only frequency to active power transfer function, but also the comprehensive transfer functions from the all possible inputs, references and grid state changes, to the outputs, real and reactive powers, including the cross couplings between them; (iii) to make use of the transfer functions to clearly relate VSG terminal performance (power overshoot and damping, settling time and oscillation frequency) to its settings and the grid characteristics. Furthermore, the analysis is used as a basis for exploring the influence of the settings on the terminal characteristics with simplified equations providing a basis for VSG design. The developed models are validated with hardware experiments. Under the parametric analysis, the VSG transient performance, including the overshoot, settling time and steady-state error can be predicted from the mathematics computation, this is verified also by the hardware experiments.

This paper first introduces the large signal model of VSG in Section 2. From this model, the transfer functions relating active and reactive powers' outputs to reference changes and grid frequency changes are developed. In Section 3, based on the transfer functions, the effects of VSG settings on its output performance will be analysed. Finally, the VSG parametric effects are validated in a hardware experiment in Section 5.

## 2 VSG large signal model

VSG control is implemented into grid-connected inverters, which typically interface the DC bus voltage from renewable generation or storage to the AC grid. The structure of the VSG consists of an active power regulation block, reactive power regulation block, virtual impedance and a conventional VSC as shown in Fig. 1. The blocks highlighted in blue form is the core of VSG control, which aims to compute the reference output voltage $u_{o,ref}$ for the VSC according to the required power; the blocks highlighted in red form

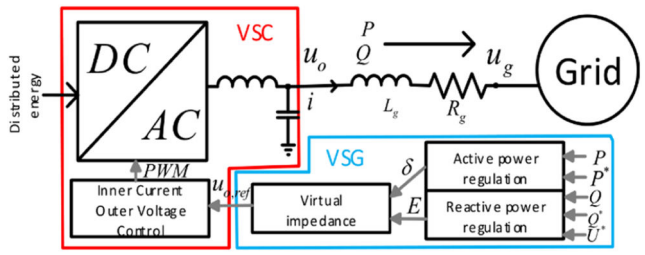


**Fig. 1** *Virtual SG control structure*

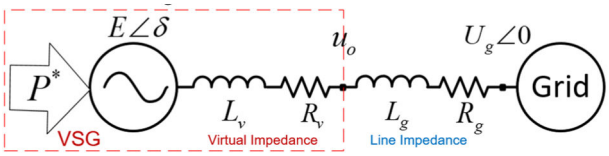


**Fig. 2** *Electrical system model of VSG connecting to the grid*

is the conventional voltage controlled VSC with output voltage $u_o$ tracking $u_{o,ref}$. In this work it is assumed that the DC link voltage is maintained constant, e.g. by the action of the controller for the storage system. It is also assumed that the response time of the VSG control is similar to that of the SG, i.e. in the range of seconds, while the VSC voltage controller response time is <10 ms. Considering this separation in response times, the large signal model neglects the fast-response VSC and only models the VSG (i.e. it essentially assumes that $u_o = u_{o,ref}$). The specific conditions under which this assumption remains valid to have been verified in [39]. It is also assumed that the VSG is connected to an infinite bus, with voltage, $\boldsymbol{u}_g$, through a line impedance, $Z_g$. Since the VSC acts as a voltage controlled converter, the electric potential $E\angle\delta$ is the controlled VSC voltage after the filter. Owing to the implementation of a virtual impedance, $E$ can be considered a virtual voltage and the actual output voltage of the VSG after the virtual impedance is $u_o$ as shown in Fig. 2.

### 2.1 Active power regulation

The active power exchanged between the VSG and the grid is determined by the angle $\delta$ of the virtual electric potential, $\boldsymbol{e}$, relative to the grid voltage angle. This angle is composed of a contribution from the reference active power setpoint which can also include a droop component for steady-state frequency support, and a contribution from inertia during transients. The inertia part is determined from the swing (1) while the droop part is determined from active power-frequency droop (2)

$$\frac{\mathrm{d}\Delta\omega_{\mathrm{VSG}}}{\mathrm{d}t} = \frac{P^*}{J} - \frac{P}{J} - \frac{D(\omega_{\mathrm{VSG}} - \omega_{\mathrm{g}})}{J} \tag{1}$$

$$P^* = P + K_{\mathrm{d}}(\omega_{\mathrm{g}} - \omega^*) \tag{2}$$

where $J$ is virtual inertia, $D$ is damping gain, $K_{\mathrm{d}}$ is droop gain, $\omega_{\mathrm{VSG}}$ is VSG frequency, $\omega_{\mathrm{g}}$ is grid frequency, $\omega^*$ is reference frequency, $P$ is VSG output active power and $P^*$ is VSG reference active power.

If the damping gain $D$ is made equal to droop gain $K_{\mathrm{d}}$, (1) and (2) can be combined as follows:

$$\frac{\mathrm{d}\Delta\omega_{\mathrm{VSG}}}{\mathrm{d}t} = \frac{P^*}{J} - \frac{P}{J} - \frac{K_{\mathrm{d}}(\omega_{\mathrm{VSG}} - \omega^*)}{J} \tag{3}$$

The constraints for the parameters $J$ and $K_{\mathrm{d}}$ to ensure stability have been analysed in [39]. Compared with the use of different damping and droop parameters, this approach has a narrower scope, since one parameter serves the purpose of damping during transients and droop during steady-state. It does have the advantage of eliminating the need for a PLL. Although the analysis here is based on (3), nevertheless, it would be possible to extend the analysis to the method with separate damping and droop with (2). This possibility is discussed later in Section 6.

### 2.2 Reactive power regulation

The reactive power exchanged between the VSG and the grid is determined by the electric potential magnitude $E$ and can incorporate a reactive power-voltage droop term as in (4) [41]

$$E = U^* + K_q(Q^* - Q) \tag{4}$$

where $K_q$ is the reactive power droop gain, $U^*$ is the voltage reference, $Q^*$ is the reactive power reference, and $Q$ is the VSG output reactive power.

### 2.3 Virtual impedance

The virtual impedance [36] $R_{\mathrm{v}} + \mathrm{j}X_{\mathrm{v}}$ plays a similar role to the stator impedance of a synchronous machine. Thus, the virtual impedance connects the VSG to the transmission line in series as shown in Fig. 2. Hence, the current through the virtual impedance

is the VSG output current $\vec{\to} \boldsymbol{i}$. Thus, the VSG output voltage $\boldsymbol{u}_o$ can be obtained as the electric potential minus the voltage drop on the virtual impedance

$$\boldsymbol{u}_o = \boldsymbol{e} - (R_v + jX_v)\boldsymbol{i} \tag{5}$$

### 2.4 Electrical system model

In steady-state, the reactive power and active power references determine the virtual electric potential and its phase angle, respectively. Assuming the transmission line impedance between the VSG and grid is $R_g + jX_g$, and the grid voltage is $\boldsymbol{u}_g$ and taking the grid voltage as the reference as defined by (8), then the resulting phase angle from the active power regulation is equal to the phase difference between the grid and the VSG potential. Then the electric potential can be defined as (6) in the static $dq$-frame, where the angle is the integral of the frequency change in both VSG and grid (7)

$$\boldsymbol{e} = e_d + je_q = E\cos(\delta) + jE\sin(\delta) \tag{6}$$

$$\frac{d\delta}{dt} = \Delta\omega_{VSG} + \Delta\omega_g \tag{7}$$

$$\boldsymbol{u}_g = u_{gd} + ju_{gq} = U_g \tag{8}$$

where $U_g$ is the magnitude of the grid voltage and $\Delta\omega_g = (\omega^* - \omega_g)$.

Fig. 2 presents the electrical system model of the VSG connected to the grid.

From Fig. 2, the output current or line current can be easily computed as

$$R = R_v + R_g \tag{9}$$

$$X = X_v + X_g = 2\pi f_{VSG}L_v + 2\pi f_g L_v \tag{10}$$

$$\boldsymbol{i} = i_d + ji_q = \frac{\boldsymbol{e} - \boldsymbol{u}_g}{R + jX} \tag{11}$$

The current in $dq$-frame would be

$$\begin{cases} i_d = \dfrac{R}{R^2+X^2}(e_d - u_{gd}) + \dfrac{X}{R^2+X^2}(e_q - u_{gq}) \\ i_q = -\dfrac{X}{R^2+X^2}(e_d - u_{gd}) + \dfrac{R}{R^2+X^2}(e_q - u_{gq}) \end{cases} \tag{12}$$

Substituting (6) into (5) gives the output voltage in the $dq$-frame

$$\begin{cases} u_{od} = E\cos\delta - i_d R_v + i_q X_v \\ u_{oq} = E\sin\delta - i_d X_v - i_q R_v \end{cases} \tag{13}$$

Equations (12) and (13) give the output current and voltage from the VSG, respectively and its power output can be computed as follows:

$$P = \frac{3}{2}(u_{od}i_d + u_{oq}i_q) \tag{14}$$

$$Q = \frac{3}{2}(-u_{od}i_q + u_{oq}i_d) \tag{15}$$

The active power $P$ computed from (14) can be viewed as the feedback for active power regulation in (3), while the reactive power $Q$ computed from (15) can be viewed as the feedback for reactive power regulation in (4). Then (3)–(15) describe the closed-loop VSG, large signal model. Fig. 3 depicts the VSG large signal model where each part from the above section is indicated in the figure. The input is the references ($P^*$, $Q^*$, $U^*$) and grid information ($U_g$, $\Delta\omega_g$), while the output is the VSG generated power or VSG output voltage and current.

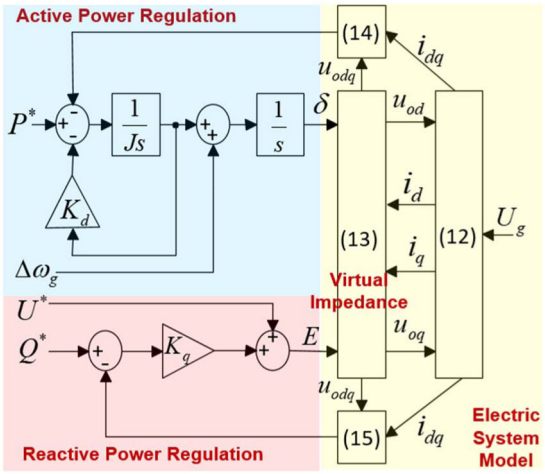


**Fig. 3** *VSG large signal model*

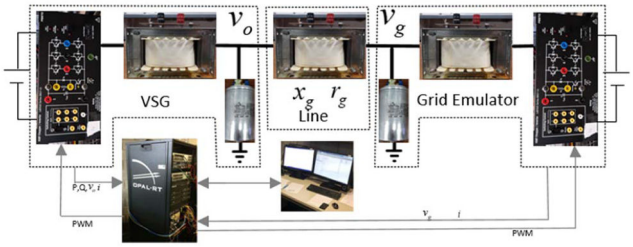


**Fig. 4** *Hardware experimental set-up*

**Table 1** Hardware VSG settings

| Parameter | Value | Parameter | Value |
|---|---|---|---|
| PWM/sampling time | 1350/14.81 × $10^{-6}$ s | filter inductance | 0.033 H |
| rated voltage $U_g$ | 100 V | filter resistance | 0.1266 Ω |
| reference voltage $U^*$ | 100 V | filter capacitance | 80 μF |
| reference angular frequency $\omega^*$ | 2π*50sHz | line inductance | 0.033 H |
| VSG inertia $J$ | 20 W/rad$^{-1}$ s$^2$ | line resistance | 1.44 Ω |
| VSG damping/ droop $K_d$ | 80 W/rad$^{-1}$s | virtual inductance | 0.011 H |
| VSG reactive power droop $K_q$ | 0.01 VA/V | virtual resistance | 0.1 Ω |
| current controller $P/I$ | 66/339.8 | voltage controller $P/I$ | 0.0535/11.987 |

### 2.5 VSG large signal model validation

To validate the accuracy of the large signal model, we compare the VSG large signal model (Fig. 3) result to measurements obtained from a hardware in the loop test of a VSG controlled converter. The hardware uses two 100 V, 2 kVA, three-phase AC/DC converters with control and measurement implemented via an OPAL-RT platform as shown in Fig. 4. Two converters are used, with one converter implementing VSG control while the other converter models the grid. These two converters use an LC filter and connect through an inductance emulating a transmission line. The parameters of the system and settings for the VSG are summarised in Table 1. The large signal model is implemented in Matlab/Simulink with the same VSG settings as given in Table 1.

Initially, both reference active power and reactive power are set to be 0 and the grid operates at 50 Hz. At 27.5 s, the reference active power step increases to 300 W, while at 27.5 s, the reference reactive power step increases to 300 Var. At 37.5 s, the grid frequency decreases to 49 Hz with 1 Hz/s ramp.

Fig. 5*a* is the output active power, while Fig. 5*b* is the output reactive power. From these results, the large signal model gives the

same performance as the hardware experiment. This hardware validation gives confidence that the large signal model can be validly used to analyse the effect of VSG settings on steady-state, settling time and overshoot when the system is subject to changes about the operating point.

## 3 Development of transfer functions

The aim of this section is to develop transfer functions, based on the large signal model, which relate the VSG inputs to outputs. The inputs to the VSG are reference active power $P^*$, reference reactive power $Q^*$ and grid frequency $\omega_g$, while the outputs from VSG are active power $P$ and reactive power $Q$. Therefore, the transfer functions of interest are:

- $G_{P\_P}$ reference active power to output active power
- $G_{Q\_P}$ reference active power to output reactive power
- $G_{P\_Q}$ reference reactive power to output active power
- $G_{Q\_Q}$ reference reactive power to output reactive power
- $G_{P\_\omega}$ grid frequency to output active power
- $G_{Q\_\omega}$ grid frequency to output reactive power.

The analysis starts by using the electrical system model equations to derive the relationships between angle, $\delta$ and potential $E$, to real and reactive powers' outputs. Since we neglect the fast VSC dynamics, these relationships are a set of gains, $H_{dP/d\delta}$, $H_{dQ/d\delta}$ which relate a change in angle to the resulting change in real and reactive powers, and $H_{dP/dE}$, $H_{dQ/dE}$ which relate a change in the potential to the resulting change in real and reactive powers. Subsequently, from the active power regulation part, the transfer function from reference active power and frequency to the angle $\delta$ can be determined. Similarly, from the reactive power part, the function from reference reactive power to potential $E$ can be determined. These can be combined with the gains to derive the overall transfer functions of interest as listed above.

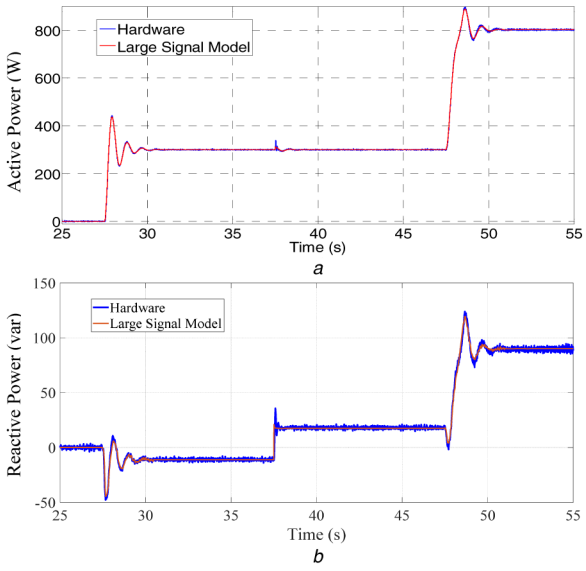


**Fig. 5** *Comparison results between hardware and large signal model*
***(a)*** Output active power, ***(b)*** Output reactive power

### 3.1 Small signal model and transfer functions

This section presents the development of the relationship of phase angle to output real and reactive powers ($H_{dP/d\delta}$, $H_{dQ/d\delta}$) and the potential to real and reactive powers ($H_{dP/dE}$, $H_{dQ/dE}$).

*3.1.1 Initial operating point:* Assuming in pre-disturbance the VSG operates at phase angle $\delta_0$, and its electric potential is $E_0$ then substituting (6) into (12) we obtain the initial current

$$\begin{cases} i_{d0} = \dfrac{(E_0\cos\delta_0 - U_g)R + E_0X\sin\delta_0}{R^2 + X^2} \\ i_{q0} = \dfrac{-(E_0\cos\delta_0 - U_g)X + E_0R\sin\delta_0}{R^2 + X^2} \end{cases} \tag{16}$$

Substituting (16) into (13) we obtain the initial output voltages as shown in the following equation: (see (17))

*3.1.2 Small signal change in angle $\Delta\delta$:* Assuming a small signal disturbance in angle, $\Delta\delta$, and in currents, $\Delta i_d$, $\Delta i_q$, substituting into (16), expanding and assuming, $\cos(\Delta\delta) \simeq 1$, and $\sin(\Delta\delta) \simeq \Delta\delta$ then we obtain

$$\begin{cases} \dfrac{\Delta i_d}{\Delta\delta} = \dfrac{-R\sin\delta_0 + X\cos\delta_0}{R^2 + X^2}E_0 \\ \dfrac{\Delta i_q}{\Delta\delta} = \dfrac{X\sin\delta_0 + R\cos\delta_0}{R^2 + X^2}E_0 \end{cases} \tag{18}$$

(see (19))

With a similar approach using (13) and (18) in (14) and (15), we can derive the transfer functions from small signal angle change to real and reactive powers change

$$H_{dP/d\delta} = \frac{\Delta P}{\Delta\delta} = \frac{3(E_0U_gR\sin\delta_0 + E_0U_gX\cos\delta_0)}{2(R^2 + X^2)} - \frac{3(E_0U_gR^2R_v\sin\delta_0 + E_0U_gX^2R_v\sin\delta_0)}{(R^2 + X^2)^2} \tag{20}$$

$$H_{dQ/d\delta} = \frac{\Delta Q}{\Delta\delta} = \frac{3(E_0U_gX\sin\delta_0 - E_0U_gR\cos\delta_0)}{2(R^2 + X^2)} - \frac{3(E_0U_gR^2X_v\sin\delta_0 + E_0U_gX^2X_v\sin\delta_0)}{(R^2 + X^2)^2} \tag{21}$$

*3.1.3 Small signal change in potential, $\Delta E$:* Following a similar procedure for the change in currents due to a change in VSG potential gives (22) and (23):

$$\begin{cases} u_{od0} = E_0\cos\delta_0 + \dfrac{-(E_0\cos\delta_0 - U_g)RR_v - E_0XR_v\sin\delta_0 - (E_0\cos\delta_0 - U_g)XX_v + E_0RX_v\sin\delta_0}{R^2 + X^2} \\ u_{oq0} = E_0\sin\delta_0 + \dfrac{(E_0\cos\delta_0 - U_g)XR_v - E_0RR_v\sin\delta_0 - (E_0\cos\delta_0 - U_g)RX_v - E_0XX_v\sin\delta_0}{R^2 + X^2} \end{cases} \tag{17}$$

$$\begin{cases} \dfrac{\Delta u_{od}}{\Delta\delta} = -E_0\sin\delta_0 + \dfrac{E_0RR_v\sin\delta_0 - E_0XR_v\cos\delta_0 + E_0XX_v\sin\delta_0 + E_0RX_v\cos\delta_0}{R^2 + X^2} \\ \dfrac{\Delta u_{oq}}{\Delta\delta} = E_0\cos\delta_0 + \dfrac{-E_0XR_v\sin\delta_0 - E_0RR_v\cos\delta_0 + E_0RX_v\sin\delta_0 - E_0XX_v\cos\delta_0}{R^2 + X^2} \end{cases} \tag{19}$$

$$\begin{cases} \dfrac{\Delta i_d}{\Delta E} = \dfrac{X\sin\delta_0 + R\cos\delta_0}{R^2 + X^2} \\ \dfrac{\Delta i_q}{\Delta E} = \dfrac{R\sin\delta_0 - X\cos\delta_0}{R^2 + X^2} \end{cases} \tag{22}$$

$$\begin{cases} \dfrac{\Delta u_{od}}{\Delta E} = \cos\delta_0 + \dfrac{-RR_v\cos\delta_0 - XR_v\sin\delta_0 - XX_v\cos\delta_0 + RX_v\sin\delta_0}{R^2 + X^2} \\ \dfrac{\Delta u_{oq}}{\Delta E} = \sin\delta_0 + \dfrac{XR_v\cos\delta_0 - RR_v\sin\delta_0 - RX_v\cos\delta_0 - XX_v\sin\delta_0}{R^2 + X^2} \end{cases} \tag{23}$$

Then the gains for potential to power can be obtained:

$$H_{dP/dE} = \frac{\Delta P}{\Delta E} = \frac{3\left(2E_0R - U_gR\cos\delta_0 + U_gX\sin\delta_0\right)}{2\left(R^2 + X^2\right)} + \frac{3\left(U_gX^2R_v\cos\delta_0 + U_gR^2R_v\cos\delta_0 - E_0X^2R_v - E_0R^2R_v\right)}{\left(R^2 + X^2\right)^2} \tag{24}$$

$$H_{dQ/dE} = \frac{\Delta Q}{\Delta E} = \frac{3\left(2E_0X - U_gX\cos\delta_0 - U_gR\sin\delta_0\right)}{2\left(R^2 + X^2\right)} + \frac{3\left(U_gX^2X_v\cos\delta_0 + U_gR^2X_v\cos\delta_0 - E_0X^2X_v - E_0R^2X_v\right)}{\left(R^2 + X^2\right)^2} \tag{25}$$

Now considering the above relationships, the closed-loop transfer function diagram can be formed as shown in Fig. 6. The inputs are reference active power change $\Delta P^*$, grid frequency change $\Delta\omega_g$ and reference reactive power change $\Delta Q^*$. The outputs are output active power change $\Delta P$ and output reactive power change $\Delta Q$.

### 3.2 Transfer functions

*3.2.1 Reference active power step change:* With reference to Fig. 6 we can now find the transfer functions from reference active power change to output active power and reactive power, assuming the grid frequency and reference reactive power are invariant i.e. $\Delta Q^* = 0$, $\Delta\omega_g = 0$. The transfer functions are $G_{P\_P}$ and $G_{Q\_P}$ as in (26) and (27).

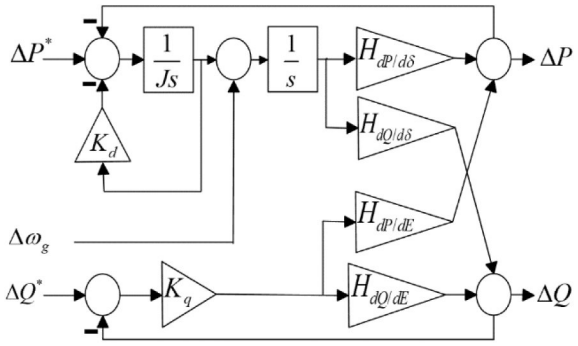


**Fig. 6** *VSG small signal closed-loop transfer function*

$$G_{P\_P} = \frac{H_{dP/d\delta} - H_{dQ/d\delta}H_{dP/dE}(K_q/(1 + K_qH_{dQ/dE}))}{Js^2 + K_ds + H_{dP/d\delta} - H_{dQ/d\delta}H_{dP/dE}(K_q/(1 + K_qH_{dQ/dE}))} \tag{26}$$

(see (27))

*3.2.2 Reference reactive power step change:* Again, with reference to Fig. 6, the transfer functions from reference reactive power change to reactive $G_{P\_Q}$ and active power output $G_{Q\_Q}$, assuming the grid frequency and reference active power are invariant ($\Delta P^* = 0$, $\Delta\omega_g = 0$) are given by (28) and (29).

(see (28))

(see (29))

*3.2.3 Grid frequency step change:* The transfer function for grid frequency change to active and reactive powers, assuming the reference reactive and reference active power is invariant or $\Delta P^* = 0$, $\Delta Q^* = 0$, are given by $G_{P\_\omega}$ and $G_{Q\_\omega}$ as (30) and (31), respectively.

$$G_{P\_f} = \frac{\left(H_{dP/d\delta} - H_{dQ/d\delta}H_{dP/dE}(K_q/(1 + K_qH_{dQ/dE}))\right)(Js + K_d)}{Js^2 + K_ds + H_{dP/d\delta} - H_{dQ/d\delta}H_{dP/dE}(K_q/(1 + K_qH_{dQ/dE}))} \tag{30}$$

$$G_{Q\_f} = \frac{(H_{dQ/d\delta}/(1 + K_qH_{dQ/dE}))(Js + K_d)}{Js^2 + K_ds + H_{dP/d\delta} - K_qH_{dP/dE}((1 + K_qH_{dQ/dE})/H_{dQ/d\delta})} \tag{31}$$

Note that all of above transfer functions (26)–(31) are second order, which arises from the fact that the work ignored the dynamics of the VSC itself on the assumption that they are much faster than the VSG controls.

### 3.3 Steady-state values

It is interesting to examine the steady-state value of the active and reactive powers, after a change in inputs or grid frequency. These steady-state values can easily be obtained from (26)–(31) by setting $s = 0$ and are summarised in Table 2. From Table 2, it is obvious that in steady-state the output active power can fully follow the reference active power, is decoupled from the reference reactive power and droops the active power according to the frequency change. However, the output reactive power is coupled with the reference active power and does not even fully follow the reference reactive power. Essentially this is because the active power control loop has an integrator as part of the swing equation thus forcing zero steady-state error, while the reactive power control loop only has a proportional gain or droop term.

### 3.4 Damping ratios and natural oscillation

For the second-order transfer functions, the damping ratios and natural oscillation frequency can be computed, which can then further be used to determine settling times and overshoot.

Table 3 gives the damping ratio and natural oscillation frequency for all the transfer functions.

In $G_{P\_P}$ and $G_{P\_\omega}$, since reactive power is always positively associated with electric potential, $H_{dQ/dE} > 0$, thus,

$$G_{Q\_P} = \frac{H_{dQ/d\delta}}{J\left(1 + K_qH_{dQ/dE}\right)s^2 + K_d\left(1 + K_qH_{dQ/dE}\right)s + \left(H_{dQ/d\delta}H_{dP/dE}/H_{dQ/dE}\right) + H_{dP/d\delta}\left(1 + K_qH_{dQ/dE}\right)} \tag{27}$$

$$G_{P\_\omega} = \frac{JK_qH_{dP/dE}s^2 + K_dK_qH_{dP/dE}s}{J\left(1 + K_qH_{dQ/dE}\right)s^2 + K_d\left(1 + K_qH_{dQ/dE}\right)s + H_{dP/d\delta} + \left(H_{dP/d\delta} - H_{dQ/d\delta}\right)K_qH_{dP/dE}} \tag{28}$$

$$G_{Q\_\omega} = \frac{JK_qH_{dQ/dE}s^2 + K_dK_qH_{dQ/dE}s + H_{dP/d\delta}K_qH_{dQ/dE} - H_{dQ/d\delta}K_qH_{dP/dE}}{J\left(1 + K_qH_{dQ/dE}\right)s^2 + K_d\left(1 + K_qH_{dQ/dE}\right)s + H_{dP/d\delta} + H_{dP/d\delta}K_qH_{dQ/dE} - H_{dQ/d\delta}K_qH_{dP/dE}} \tag{29}$$

**Table 2** Steady-state value and overshoot

| Transfer function | Steady-state value $S$ | Overshoot $PO$ |
|---|---|---|
| $G_{P\_P}$ | 1 | $\left(\exp\left(-\frac{\xi\pi}{\sqrt{1-\xi^2}}\right)+1\right)$ |
| $G_{Q\_P}$ | $\frac{H_{\mathrm{d}Q/\mathrm{d}\delta}}{\frac{H_{\mathrm{d}Q/\mathrm{d}\delta}H_{\mathrm{d}P/\mathrm{d}E}}{H_{\mathrm{d}Q/\mathrm{d}E}}+H_{\mathrm{d}P/\mathrm{d}\delta}\left(1+K_qH_{\mathrm{d}Q/\mathrm{d}E}\right)}$ | $\left(\exp\left(-\frac{\xi\pi}{\sqrt{1-\xi^2}}\right)+1\right)*\frac{H_{\mathrm{d}Q/\mathrm{d}\delta}}{\frac{H_{\mathrm{d}Q/\mathrm{d}\delta}H_{\mathrm{d}P/\mathrm{d}E}}{H_{\mathrm{d}Q/\mathrm{d}E}}+H_{\mathrm{d}P/\mathrm{d}\delta}\left(1+K_qH_{\mathrm{d}Q/\mathrm{d}E}\right)}$ |
| $G_{P\_Q}$ | 0 | $\frac{K_qH_{\mathrm{d}P/\mathrm{d}E}}{1+K_qH_{\mathrm{d}Q/\mathrm{d}E}}$ |
| $G_{Q\_Q}$ | $\frac{H_{\mathrm{d}P/\mathrm{d}\delta}K_qH_{\mathrm{d}Q/\mathrm{d}E}-H_{\mathrm{d}Q/\mathrm{d}\delta}K_qH_{\mathrm{d}P/\mathrm{d}E}}{H_{\mathrm{d}P/\mathrm{d}\delta}+H_{\mathrm{d}P/\mathrm{d}\delta}K_qH_{\mathrm{d}Q/\mathrm{d}E}-H_{\mathrm{d}Q/\mathrm{d}\delta}K_qH_{\mathrm{d}P/\mathrm{d}E}}$ | $\frac{K_qH_{\mathrm{d}Q/\mathrm{d}E}}{1+K_qH_{\mathrm{d}Q/\mathrm{d}E}}$ |
| $G_{P\_\omega}$ | $K_d$ | $\frac{c_1}{\omega_{P\_\omega}}\mathrm{e}^{-a_{P\_\omega}\cdot t_{P\_\omega}}\sin(\omega_{P\_\omega}\cdot t_{P\_\omega})+K_d\left(1-\mathrm{e}^{-a_{P\_\omega}\cdot t_{P\_\omega}}\cos(\omega_{P\_\omega}\cdot t_{P\_\omega})-\frac{a_{P\_\omega}}{\omega_{P\_\omega}}\mathrm{e}^{-a_{P\_\omega}\cdot t}\sin(\omega_{P\_\omega}\cdot t_{p\_\omega})\right)$ |
| $G_{Q\_\omega}$ | $\frac{H_{\mathrm{d}Q/\mathrm{d}\delta}K_d}{\left(1+K_qH_{\mathrm{d}Q/\mathrm{d}E}\right)H_{\mathrm{d}P/\mathrm{d}\delta}-K_qH_{\mathrm{d}P/\mathrm{d}E}\frac{\left(1+K_qH_{\mathrm{d}Q/\mathrm{d}E}\right)^2}{H_{\mathrm{d}Q/\mathrm{d}\delta}}}$ | $\frac{c_2}{\omega_{Q\_\omega}}e^{-a_{Q\_\omega}\cdot t_{Q\_\omega}}\sin(\omega_{Q\_\omega}\cdot t_{Q\_\omega})+\frac{K_dc_2}{c_3}\left(1-e^{-a_{Q\_\omega}\cdot t_{p\_\omega}}\cos(\omega_{Q\_\omega}\cdot t_{Q\_\omega})-\frac{a_{Q\_\omega}}{\omega_{Q\_\omega}}e^{-a_{Q\_\omega}\cdot t_{Q\_\omega}}\sin(\omega_{Q\_\omega}\cdot t_{Q\_\omega})\right)$ |

**Table 3** Damping ratio and natural oscillation frequency

| Transfer function | Damping ratio $\xi$ | Natural oscillation frequency $\omega_n$ |
|---|---|---|
| $G_{P\_P}$ | $\frac{K_d}{2\sqrt{J\left(H_{\mathrm{d}P/\mathrm{d}\delta}-H_{\mathrm{d}Q/\mathrm{d}\delta}H_{\mathrm{d}P/\mathrm{d}E}\frac{K_q}{1+K_qH_{\mathrm{d}Q/\mathrm{d}E}}\right)}}$ | $\sqrt{\left(H_{\mathrm{d}P/\mathrm{d}\delta}-H_{\mathrm{d}Q/\mathrm{d}\delta}H_{\mathrm{d}P/\mathrm{d}E}\frac{K_q}{1+K_qH_{\mathrm{d}Q/\mathrm{d}E}}\right)/J}$ |
| $G_{Q\_P}$ | $\frac{K_d\left(1+K_qH_{\mathrm{d}Q/\mathrm{d}E}\right)}{2\sqrt{J\left(1+K_qH_{\mathrm{d}Q/\mathrm{d}E}\right)\left(\frac{H_{\mathrm{d}Q/\mathrm{d}\delta}H_{\mathrm{d}P/\mathrm{d}E}}{H_{\mathrm{d}Q/\mathrm{d}E}}+H_{\mathrm{d}P/\mathrm{d}\delta}\left(1+K_qH_{\mathrm{d}Q/\mathrm{d}E}\right)\right)}}$ | $\sqrt{\left(\frac{H_{\mathrm{d}Q/\mathrm{d}\delta}H_{\mathrm{d}P/\mathrm{d}E}}{H_{\mathrm{d}Q/\mathrm{d}E}}+H_{\mathrm{d}P/\mathrm{d}\delta}\left(1+K_qH_{\mathrm{d}Q/\mathrm{d}E}\right)\right)/\left(J\left(1+K_qH_{\mathrm{d}Q/\mathrm{d}E}\right)\right)}$ |
| $G_{P\_Q}$ | $\frac{K_d\left(1+K_qH_{\mathrm{d}Q/\mathrm{d}E}\right)}{2\sqrt{J\left(1+K_qH_{\mathrm{d}Q/\mathrm{d}E}\right)\left(H_{\mathrm{d}P/\mathrm{d}\delta}+\left(H_{\mathrm{d}P/\mathrm{d}\delta}-H_{\mathrm{d}Q/\mathrm{d}\delta}\right)K_qH_{\mathrm{d}P/\mathrm{d}E}\right)}}$ | $\sqrt{\left(H_{\mathrm{d}P/\mathrm{d}\delta}+\left(H_{\mathrm{d}P/\mathrm{d}\delta}-H_{\mathrm{d}Q/\mathrm{d}\delta}\right)K_qH_{\mathrm{d}P/\mathrm{d}E}\right)/\left(J\left(1+K_qH_{\mathrm{d}Q/\mathrm{d}E}\right)\right)}$ |
| $G_{Q\_Q}$ | $\frac{K_d\left(1+K_qH_{\mathrm{d}Q/\mathrm{d}E}\right)}{2\sqrt{J\left(1+K_qH_{\mathrm{d}Q/\mathrm{d}E}\right)\left(H_{\mathrm{d}P/\mathrm{d}\delta}+H_{\mathrm{d}P/\mathrm{d}\delta}K_qH_{\mathrm{d}Q/\mathrm{d}E}-H_{\mathrm{d}Q/\mathrm{d}\delta}K_qH_{\mathrm{d}P/\mathrm{d}E}\right)}}$ | $\sqrt{\left(H_{\mathrm{d}P/\mathrm{d}\delta}+H_{\mathrm{d}P/\mathrm{d}\delta}K_qH_{\mathrm{d}Q/\mathrm{d}E}-H_{\mathrm{d}Q/\mathrm{d}\delta}K_qH_{\mathrm{d}P/\mathrm{d}E}\right)/\left(J\left(1+K_qH_{\mathrm{d}Q/\mathrm{d}E}\right)\right)}$ |
| $G_{P\_\omega}$ | $\frac{K_d}{2\sqrt{J\left(H_{\mathrm{d}P/\mathrm{d}\delta}-H_{\mathrm{d}Q/\mathrm{d}\delta}H_{\mathrm{d}P/\mathrm{d}E}\frac{K_q}{1+K_qH_{\mathrm{d}Q/\mathrm{d}E}}\right)}}$ | $\sqrt{\left(H_{\mathrm{d}P/\mathrm{d}\delta}-H_{\mathrm{d}Q/\mathrm{d}\delta}H_{\mathrm{d}P/\mathrm{d}E}\frac{K_q}{1+K_qH_{\mathrm{d}Q/\mathrm{d}E}}\right)/J}$ |
| $G_{Q\_\omega}$ | $\frac{K_d\left(1+K_qH_{\mathrm{d}Q/\mathrm{d}E}\right)}{2\sqrt{J\left(1+K_qH_{\mathrm{d}Q/\mathrm{d}E}\right)\left(\frac{H_{\mathrm{d}Q/\mathrm{d}\delta}H_{\mathrm{d}P/\mathrm{d}E}}{H_{\mathrm{d}Q/\mathrm{d}E}}+H_{\mathrm{d}P/\mathrm{d}\delta}\left(1+K_qH_{\mathrm{d}Q/\mathrm{d}E}\right)\right)}}$ | $\sqrt{\left(\frac{H_{dQ/\mathrm{d}\delta}H_{dP/dE}}{H_{dQ/dE}}+H_{dP/\mathrm{d}\delta}\left(1+K_qH_{dQ/dE}\right)\right)/\left(J\left(1+K_qH_{dQ/dE}\right)\right)}$ |

$K_q/(1+K_qH_{\mathrm{d}Q/\mathrm{d}E})<K_q$. Actually, according to (4), $K_q<(U_{\max}-U_{\min})/(P_{\max}-P_{\min})$, so that $K_q$ would typically be a small value. The effect of angle to reactive power and voltage to active power is normally small, assuming large inductance to resistance ratio. Thus $H_{\mathrm{d}P/\mathrm{d}\delta}\gg H_{\mathrm{d}Q/\mathrm{d}\delta}H_{\mathrm{d}P/\mathrm{d}E}K_q$. Therefore, the damping ratio of $G_{P\_P}$ and $G_{P\_\omega}$ can be simplified as $K_d/2\sqrt{JH_{\mathrm{d}P/\mathrm{d}\delta}}$.

In $G_{Q\_P}$ and $G_{Q\_\omega}$, similarly, $H_{\mathrm{d}Q/\mathrm{d}\delta}H_{\mathrm{d}P/\mathrm{d}E}/H_{\mathrm{d}Q/\mathrm{d}E}\ll H_{\mathrm{d}P/\mathrm{d}\delta}$. Thus, the damping ratio of $G_{Q\_P}$ and $G_{Q\_\omega}$ can be simplified as $K_d/2\sqrt{JH_{\mathrm{d}P/\mathrm{d}\delta}}$.

In $G_{P\_Q}$, $H_{\mathrm{d}P/\mathrm{d}\delta}\gg H_{\mathrm{d}Q/\mathrm{d}\delta}$ and as mentioned above, $K_q$ is small enough that

$$K_qH_{\mathrm{d}P/\mathrm{d}E}\simeq K_qH_{\mathrm{d}Q/\mathrm{d}E}.$$

Thus, $H_{\mathrm{d}P/\mathrm{d}\delta}+\left(H_{\mathrm{d}P/\mathrm{d}\delta}-H_{\mathrm{d}Q/\mathrm{d}\delta}\right)K_qH_{\mathrm{d}P/\mathrm{d}E}\simeq H_{\mathrm{d}P/\mathrm{d}\delta}\left(1+K_qH_{\mathrm{d}Q/\mathrm{d}E}\right)$. Therefore, $G_{P\_Q}$ can be simplified as $K_d/2\sqrt{JH_{\mathrm{d}P/\mathrm{d}\delta}}$.

In $G_{Q\_Q}$, $H_{\mathrm{d}P/\mathrm{d}\delta}\gg H_{\mathrm{d}Q/\mathrm{d}\delta}H_{\mathrm{d}P/\mathrm{d}E}K_q$, and $K_qH_{\mathrm{d}P/\mathrm{d}E}\simeq K_qH_{\mathrm{d}Q/\mathrm{d}E}$. Thus,

$$H_{\mathrm{d}P/\mathrm{d}\delta}+H_{\mathrm{d}P/\mathrm{d}\delta}K_qH_{\mathrm{d}Q/\mathrm{d}E}-H_{\mathrm{d}Q/\mathrm{d}\delta}K_qH_{\mathrm{d}P/\mathrm{d}E}\simeq H_{\mathrm{d}P/\mathrm{d}\delta}\left(1+K_qH_{\mathrm{d}Q/\mathrm{d}E}\right).$$

Therefore, $G_{Q\_Q}$ can be simplified as $K_d/2\sqrt{JH_{\mathrm{d}P/\mathrm{d}\delta}}$.

In total, the damping ratio for all of the mentioned second-order transfer functions can be uniformly simplified as $K_d/2\sqrt{JH_{\mathrm{d}P/\mathrm{d}\delta}}$, under the assumption that $H_{\mathrm{d}P/\mathrm{d}\delta}\gg H_{\mathrm{d}Q/\mathrm{d}\delta}H_{\mathrm{d}P/\mathrm{d}E}K_q$, $H_{\mathrm{d}Q/\mathrm{d}\delta}H_{\mathrm{d}P/\mathrm{d}E}/H_{\mathrm{d}Q/\mathrm{d}E}\ll H_{\mathrm{d}P/\mathrm{d}\delta}$ and $K_qH_{\mathrm{d}P/\mathrm{d}E}-K_qH_{\mathrm{d}Q/\mathrm{d}E}\simeq 0$ or in the case of a largely inductive line.

Similar terms occur in the expressions for the natural oscillation frequency and thus, the simplification used for the damping ratio analysis can directly be applied also to the natural oscillation frequency analysis. Therefore, the natural oscillation frequency of all of the mentioned second-order transfer function can be reduced to $\sqrt{H_{\mathrm{d}P/\mathrm{d}\delta}/J}$.

Considering that the damping ratio and natural oscillation frequency have now been defined, the system stability condition, settling time and overshoot can be computed.

*3.4.1 System stability condition:* For a second-order transfer function, the stable condition is that the damping ratio $\xi$ must be greater than zero, i.e. in this case:

$$\frac{K_d}{2\sqrt{JH_{\mathrm{d}P/\mathrm{d}\delta}}}>0 \tag{32}$$

Since damping/droop gain $K_d$ and inertia $J$ are always positive, the system would be stable as long as $H_{\mathrm{d}P/\mathrm{d}\delta}$ is positive i.e. (20) is greater than zero, which depends on initial equilibrium point, line and virtual impedance. To ensure a positive value of $H_{\mathrm{d}P/\mathrm{d}\delta}$, the angle $\delta_0$ should not exceed 90° and the total impedance $X$ should not be less than zero.

*3.4.2 Settling time:* When the system stability condition is satisfied, the settling time can be calculated based on the damping ratio $\xi$.

When $0 < \xi < 1$, the system is underdamped. The settling time $t_s$ to 2% steady-state error is

$$t_s = \frac{1}{\omega_n \xi} \log\left(\frac{1}{0.02\sqrt{1-\xi^2}}\right) \tag{33a}$$

$$t_s = \frac{2J}{K_d} \log\left(\frac{1}{0.02\sqrt{1 - K_d^2/4JH_{dP/d\delta}}}\right) \tag{33b}$$

When $\xi > 1$, the system is overdamped. The settling time $t_s$ to 2% steady-state error is

$$t_s = 4\sqrt{T_1^2 + T_2^2} \tag{34}$$

where $T_1$ and $T_2$ are the time constant of the real roots of the overdamped second-order transfer function.

$$T_1, T_2 = -\frac{1}{-\omega_n \xi \pm \omega_n \sqrt{\xi^2 - 1}} \tag{35a}$$

$$T_1, T_2 = \frac{2J}{K_d \mp \sqrt{K_d^2 - 4JH_{dP/d\delta}}} \tag{35b}$$

*3.4.3 Overshoot:* When the system is underdamped, it gives rise to overshoot during transients. The transfer function (26) is in the standard second order format and (27), (30), (31) can be transformed to standard second order format by multiplying by its steady-state value $S$. However, (28) and (29) cannot be transformed to a standard second order format. For those transfer functions in standard second order format, the overshoot can be easily computed, while for those non-standard transfer functions, the overshoot can be calculated from the definition (detailed in Appendix).

Table 2 presents the result of overshoot for all the considered transfer functions.

### 3.5 Transfer function validation

To validate the transfer function, the results obtained from the transfer function are compared to those obtained from the previously validated large signal model by the means of Matlab-based simulations. Fig. 6 shows the results for a step change in reference active power (Fig. 6*a*), reference reactive power (Fig. 6*b*), and frequency (Fig. 6*c*) where the frequency changes by 0.01 Hz (0.02π rad) with 1 Hz/s slope. The system parameters and settings are the same as in Table 1. The results of output active and reactive powers are shown in Fig. 7.

From the results, the transfer function is accurate. The output active power can precisely follow the reference, while the output reactive power as expected, couples with input reference active power and mismatches its reference.

The following validation is to confirm the calculation of steady-state value $S$ and overshoot $PO$, and compare the settling time $t_s$ damping ratio $\xi$ and natural oscillation frequency $\omega_n$ obtained from each transfer function to the simplified values. The results are shown in Table 4.

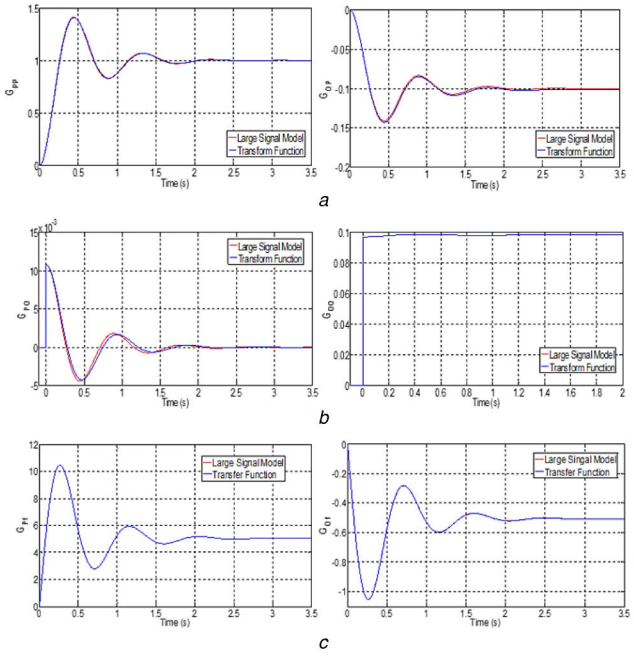


**Fig. 7** *Response from transfer function analysis compared to results from large signal model*
***(a)*** Input reference active power step change, ***(b)*** Input reference reactive power step change, ***(c)*** Input grid frequency 1 Hz/s slope change

**Table 4** System performance parameters obtained from the transfer functions and comparison with values from simplified expressions

| Transfer function | S | PO | $\xi$ | $\omega_n$ | $t_s$ |
|---|---|---|---|---|---|
| $G_{P\_P}$ | 1 | 1.41 | 0.2730 | 7.3251 | 1.9754 |
| $G_{Q\_P}$ | −0.1018 | −0.1432 | 0.2747 | 7.2795 | 1.9756 |
| $G_{P\_Q}$ | 0 | 0.0108 | 0.2856 | 7.0033 | 1.9773 |
| $G_{Q\_Q}$ | 0.0979 | 0.0968 | 0.2730 | 7.3251 | 1.9754 |
| $G_{P\_\omega}$ | 5.0265 | 10.5201 | 0.2730 | 7.3251 | 1.9754 |
| $G_{Q\_\omega}$ | −0.5055 | −1.0530 | 0.2747 | 7.2795 | 1.9756 |
| simplified | — | — | 0.2732 | 7.3207 | 1.9754 |

Comparing the results in Table 4 (steady-state $S$, overshoot $PO$ and settling time $t_s$) and Fig. 7, the expressions used in Tables 2 and 3 are validated. Comparing the calculation using the simplified expressions with the full expressions, the simplified expression for damping ratio $K_d/2\sqrt{JH_{dP/d\delta}}$, natural oscillation frequency $\sqrt{H_{dP/d\delta}/J}$ and settling time (33)–(35) are a good approximation.

With the understanding gained from the analysis of the VSG input–output transfer functions, the behaviour of VSG can be fully predicted.

## 4 Analysis of effects of VSG settings

Clearly, the VSG parameters determine its performance, and now based on the derived transfer functions we can fully analyse the effects of the various VSG settings on the performance. From the above performance parameter analysis of steady-state value, settling time and overshoot, the gains of power to angle and electric potential $H_{dP/d\delta}, H_{dQ/d\delta}, H_{dP/dE}$ and $H_{dQ/dE}$, the inertia $J$, damping/droop gain $K_d$ and reactive power droop gain $K_q$ are critical. For any given VSG, we will assume that the line impedance is fixed. The design variables are therefore the VSG settings, i.e. virtual impedance, inertia and damping/droop. To illustrate the effects of the various settings, the paper uses the example used in Table 1 to illustrate the relationships.

### 4.1 Virtual impedance effects

The virtual impedance essentially emulates the existence of an extra impedance in series with the line impedance. Owing to the fact that it is implemented via a control algorithm, the virtual impedance can be positive (increase the impedance between potential and grid) or negative. The virtual impedance directly influences the values of $H_{dP/d\delta}, H_{dQ/d\delta}, H_{dP/dE}$ and $H_{dQ/dE}$ in (20), (21), (24) and (25), respectively. These values subsequently determine the steady-state value, settling time and overshoot and it will be shown that after simplification, $H_{dP/d\delta}$ dominates the settling time and overshoot. Thus it is important to firstly analyse the effect of the virtual impedance on the gains, $H_{dP/d\delta}, H_{dQ/d\delta}, H_{dP/dE}$ and $H_{dQ/dE}$ as shown in Fig. 8. Although, these values are also dependent on the initial angle $\delta_0$ and initial potential $E_0$, the effect of both $\delta_0$ and $E_0$ are to scale (20), (21), (24) and (25) so that they would not change the shape of the curves in Fig. 8.

From Fig. 8, it can be seen that all of the gains are sensitive to the virtual inductance. Moreover, reducing the virtual inductance can increase all the gains. This result has already been verified in [42] and accords with the well-known power exchange equations

$$P = \frac{EU_g(R\cos\delta + X\sin\delta) - RU_g^2}{R^2 + X^2} \tag{36}$$

$$Q = \frac{EU_g(X\cos\delta - R\sin\delta) - XU_g^2}{R^2 + X^2} \tag{37}$$

where from (36) and (37) it is clearly seen that the inductance reduction would increase both active and reactive power flow.

*4.1.1 Virtual impedance effect on steady-state value:* Damping and inertia only affects the transient behaviour, while the steady-state performance is only related to the impedance and droop. From Table 2, it can be seen that the output active power is fully controllable, i.e. its transfer function has zero steady-state error. Thus, its steady-state value is independent of the VSG settings. In contrast, the output reactive power is only partially controllable, and its transfer function has a certain steady-state error. Its steady-state value is dependent on the virtual impedance as well as line impedance. Therefore, in steady-state analysis, we focus on reactive power or $S_{G\_P}$, $S_{G\_Q}$ ($S_{G\_f} \simeq K_d S_{G\_P}$). Fig. 9 illustrates the steady-state reactive power with reference to active power change.

As shown in Fig. 9, the virtual inductance increase and virtual resistance reduction could reduce the absolute value of $S_{G\_P}$. This reflects the fact that the increased $X/R$ ratio helps decouple the reactive and active powers [43].

Similarly, we can obtain the steady-state reactive power change with reference reactive power change as shown in Fig. 10. Impedance reduction can increase reactive power output as can be deduced in (37), while the increased reactive power would result in a reduced electric potential according to (4). Consequently, this will reduce the reactive power in (37). Hence, the reactive power has a maximum value as shown in Fig. 10*b*.

*4.1.2 Virtual impedance effect on settling time:* The settling time can be calculated from (33)–(35) and is only related to $H_{dP/d\delta}$. Settling time is calculated by two different methods, depending on the damping ratio value.

When $0 < \xi < 1$, the settling time is computed from (33b). For $\sqrt{1 - (K_d^2/4JH_{dP/d\delta})} \leq 1$, (33b) becomes:

$$t_s = \frac{2J}{K_d}\log\left(\frac{1}{0.02\sqrt{1 - K_d^2/(4JH_{dP/d\delta})}}\right) \geq \frac{2J\log 50}{K_d} \tag{38}$$

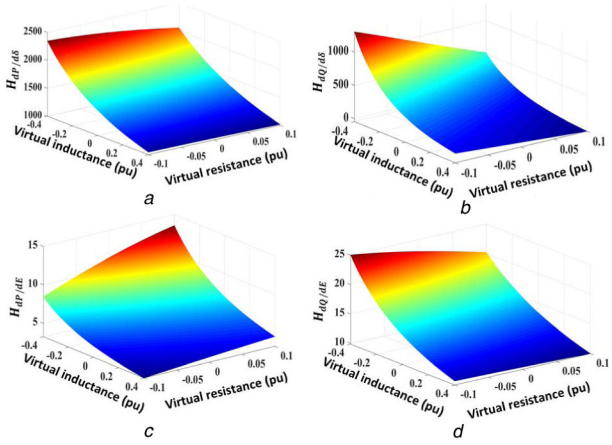


**Fig. 8** *Virtual impedance effects on H, $Z_{base}$ = 10 Ω, $X_g$ = 1.038 pu and $R_g$ = 0.144 pu*

***(a)*** Active power to angle change, ***(b)*** Reactive power to angle change, ***(c)*** Active power to potential change, ***(d)*** Reactive power to potential change

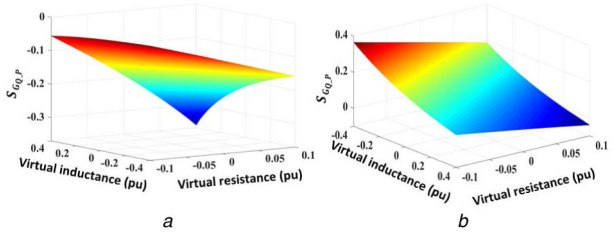


**Fig. 9** *Virtual impedance effects on $S_{G\_P}$, $Z_{base}$ = 10 Ω, $X_g$ = 1.038 pu and $R_g$ = 0.144 pu*

***(a)*** $\delta_0$–0 rad, ***(b)*** $\delta_0$–0.2793 rad

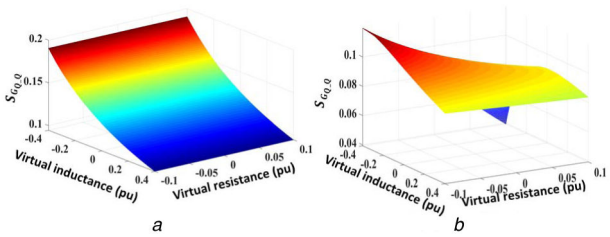


**Fig. 10** *Virtual impedance effects on $S_{G\_Q}$, $Z_{base}$ = 10 Ω, $X_g$ = 1.038 pu and $R_g$ = 0.144 pu*

***(a)*** $\delta_0$–0 rad, ***(b)*** $\delta_0$–0.2793 rad

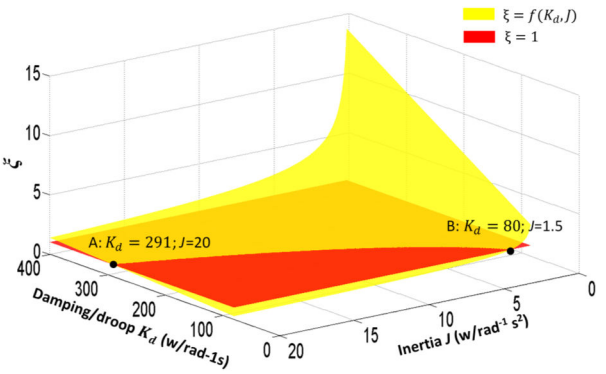


**Fig. 11** *Effects of droop/damping gain $K_d$ and inertia $J$ on settling time on damping ratio $\xi$*

The increased $H_{\mathrm{d}P/\mathrm{d}\delta}$ makes damping ratio $\sqrt{1-(K_d^2/4JH_{\mathrm{d}P/\mathrm{d}\delta})}$ approach 1, which makes $t_s$ approach $2J\log 50/K_d$ and increased $H_{\mathrm{d}P/\mathrm{d}\delta}$ reduces settling time.

When $\xi > 1$, the settling time is computed from (34) and (35b). To satisfy $\xi > 1$, $K_d$ should be greater than $2\sqrt{JH_{\mathrm{d}P/\mathrm{d}\delta}}$. Thus, in (35b), $t_s$ is dominated by $T_1$, where

$$t_s \simeq 4T_1 = \frac{8J}{K_d - \sqrt{K_d^2 - 4JH_{\mathrm{d}P/\mathrm{d}\delta}}} \tag{39}$$

The decreased $H_{\mathrm{d}P/\mathrm{d}\delta}$ makes $\sqrt{K_d^2 - 4JH_{\mathrm{d}P/\mathrm{d}\delta}}$ approach $K_d$, which makes $t_s$ approach infinity and decreased $H_{\mathrm{d}P/\mathrm{d}\delta}$ increases the settling time.

In summary, whatever $\xi$ is, as long as it is stable increasing $H_{\mathrm{d}P/\mathrm{d}\delta}$ would reduce settling time.

*4.1.3 Overshoot:* When the system is damped with $0 < \xi < 1$, overshoot arises during the transient. This overshoot may damage the converters, due to the overload. For the second-order transfer function, its overshoot is only related to its damping ratio. As mentioned before, increasing $H_{\mathrm{d}P/\mathrm{d}\delta}$ reduces damping ratio, which will increase the overshoot. Thus, reducing virtual inductance will result in overshoot increasing.

### *4.2 Virtual inertia and droop/damping effects*

As mentioned in Section 2, it is common in VSG design, to make droop and damping gains (in swing equation) equal, thus $K_d$ has both a droop feature and damping feature. Droop only influences VSG steady-state performance, such as the steady-state, while damping only influences VSG dynamic performance, such as the damping ratio of the second-order transfer function, the settling time and overshoot. It is obvious that increasing $K_d$ can increase the power output after grid frequency changes arising from the droop feature of $K_d$. However, the transient response of the VSG associated with $K_d$ and inertia $J$ is complex. This section will focus on the damping feature of $K_d$ as well as its coordination with inertia $J$.

*4.2.1 Effect of $K_d$ and $J$ on damping ratio and natural oscillation frequency:* The inertia $J$ and the damping feature of $K_d$ only have effect on the VSG transient performance. The critical factors for the VSG transient performance based on the second order model are the damping ratio and natural oscillation frequency. Both the damping ratio and natural oscillation frequency can be simplified to $K_d/2\sqrt{JH_{\mathrm{d}P/\mathrm{d}\delta}}$ and $\sqrt{H_{\mathrm{d}P/\mathrm{d}\delta}/J}$, respectively. This makes it clearer that the damping ratio is proportional to $K_d$, while both damping ratio and natural oscillation frequency are inversely related to the square root of inertia $J$.

As usual for a second order system, the value of damping ratio $\xi$ has important impacts on the VSG transient behaviour, i.e. $\xi>1$ overdamped, $1>\xi>0$ underdamped, $0>\xi$ unstable. From $\xi = K_d/2\sqrt{JH_{\mathrm{d}P/\mathrm{d}\delta}}$, since the active power to angle gain $H_{\mathrm{d}P/\mathrm{d}\delta}$ is normally positive as aforementioned, as long as both $K_d > 0$ and $J > 0$, the system is stable. The effect of $K_d$ and $J$ on damping ratio $\xi$ is shown by the yellow surface in Fig. 11, where the red plane represents critical damping, $\xi = 1$. For this plot, $H_{\mathrm{d}P/\mathrm{d}\delta} = 1059$ as calculated from the settings in Table 1 and (20) with initial angle $\delta_0 = 0.2793$ and initial potential $E_0 = 100$. As expected, $\xi$, is proportional to $K_d$ while $\xi$ is inverse proportional to $J$. Note as the inertia $J$ approaches to 0, $\xi$ approaches to infinity. However, it should be noted that when $J$ equals zero, all the transfer functions (see (26)–(31)) become first order where only the droop part is of relevance.

*4.2.2 Settling time:* Settling time is sensitive to the damping ratio, where as shown, the damping ratio depends on the interaction between the droop/damping gains $K_d$ and inertia $J$. Thus, we separately analyse the effect of $K_d$ and $J$ on settling time.

Firstly, consider the effect of $K_d$ on settling time $t_s$ assuming $J$ is fixed. When the system is underdamped ($1>\xi>0$), according to (38), $K_d$ is inversely proportional to $t_s$. Thus, increasing droop/damping gain results in settling time reduction.

However, when the system is overdamped ($\xi>1$), according to (39), the effect of $K_d$ is more complex. Taking the derivative of $K_d - \sqrt{K_d^2 - 4JH_{\mathrm{d}P/\mathrm{d}\delta}}$:

$$\left(K_d - \sqrt{K_d^2 - 4JH_{\mathrm{d}P/\mathrm{d}\delta}}\right)' = 1 - 2K_d\left(K_d^2 - 4JH_{\mathrm{d}P/\mathrm{d}\delta}\right)^{-1/2} \tag{40a}$$

$$1 - 2K_d\left(K_d^2 - 4JH_{\mathrm{d}P/\mathrm{d}\delta}\right)^{-1/2} < 1 - 2K_d\left(K_d^2\right)^{-1/2} = -1 \tag{40b}$$

Since the derivative of $K_d - \sqrt{K_d^2 - 4JH_{\mathrm{d}P/\mathrm{d}\delta}}$ is negative, increasing $K_d$ leads to $K_d - \sqrt{K_d^2 - 4JH_{\mathrm{d}P/\mathrm{d}\delta}}$ decreasing, thus, the settling time $t_s$ increases according to (39) under the $\xi>1$ condition.

Similarly, the effect of inertia $J$ on settling time $t_s$ is directly proportional from (38) when the system is underdamped.

However, when the system is overdamped, inertia $J$ appears in both denominator and numerator part in (39). Thus, making use of *L'Hôpital* 's rule considering the derivative of the denominator and numerator part separately

$$\frac{(8J)'}{\left(K_d - \sqrt{K_d^2 - 4JH_{\mathrm{d}P/\mathrm{d}\delta}}\right)'} = \frac{8}{4H_{\mathrm{d}P/\mathrm{d}\delta}/\sqrt{K_d^2 - 4JH_{\mathrm{d}P/\mathrm{d}\delta}}} \tag{41}$$

In (41), the derivative of the denominator and numerator are both positive, however, increasing inertia $J$ will increase the derivative of the denominator. In other words, when increasing inertia $J$, the denominator part of (39) increases faster than its numerator part. Thus, the settling time will reduce with increasing inertia $J$.

*4.2.3 Overshoot:* In Table 2, when the system is underdamped, the overshoot associated with droop/damping gain $K_d$ and inertia $J$ follows from the standard second order transfer function overshoot expression $\left(\exp\left(-\xi\pi/\sqrt{1-\xi^2}\right)+1\right)$ where a reduction in damping ratio $\xi$ increases overshoot. Therefore, increasing droop/damping gain $K_d$ or reducing inertia $J$ can help decrease the overshoot.

### *4.3 Reactive power droop gain effects*

Reactive power droop gain $K_q$ has a similar effect on the potential to reactive power as the active power droop gain $K_d$ has on the angle to real power. Therefore, the main effects of $K_q$ are on the steady-state value and overshoot.

*4.3.1 Reactive power droop gain effect on steady-state:* In Table 2, only the steady-state value of $G_{Q\_P}$ (or $G_{Q\_\omega}$) and $G_{Q\_Q}$ are related to the reactive power droop gain $K_q$.

**Table 5** Increased parameter effects on VSG transient responses.

| Parameter increasing | $\xi = \frac{K_d}{2\sqrt{JH_{\mathrm{d}P/\mathrm{d}\delta}}}$ | $0 < \xi < 1$ | | $1 < \xi$ |
|---|---|---|---|---|
| | | Settling time $t_s$ | Overshoot $PO_G$ | Settling time $t_s$ |
| virtual impedance | increase | increase | reduce | increase |
| virtual inertia $J$ | reduce | increase | increase | reduce |
| virtual damping $K_d$ | increase | Reduce | reduce | reduce |
| voltage droop $K_q$ | — | — | increase | — |
| comments | increase $X/R$ ratio and $K_q$ help decouple the reactive and active powers. | | | |

Owing to $H_{\mathrm{d}Q/\mathrm{d}E} > 0$, increasing $K_q$ leads to a reduction in $S_{G_{Q\_P}}$, while it results in an increase in $S_{G_{Q\_Q}}$. Hence, increasing $K_q$ helps to, decouple reactive power from active power.

#### *4.3.2 Reactive power droop gain effect on overshoot:*

Increasing $K_q$ makes $\mathrm{PO}_{G_{P\_Q}}$ an approach $H_{\mathrm{d}P/\mathrm{d}E}/H_{\mathrm{d}Q/\mathrm{d}E}$, and makes $\mathrm{PO}_{G_{Q\_Q}}$ approach 1, while decreasing $K_q$ makes $\mathrm{PO}_{G_{\mathrm{P}\_Q}}$ approach $K_q H_{\mathrm{d}P/\mathrm{d}E}$, and makes $\mathrm{PO}_{G_{Q\_Q}}$ an approach $K_q H_{\mathrm{d}Q/\mathrm{d}E}$. Therefore, decreasing $K_q$ helps reduce overshoot.

### *4.4 Summary*

The above analysis gives some useful insight into how VSG control might be designed when applied to, for example, a storage system. Table 5 summarises the parametric effects on transient responses. The design of such a system might start from the requirement to achieve a given droop response, thus fixing $K_d$, as this determines steady-state output in reaction to a frequency change and therefore largely impacts the storage capacity. As regards dynamic response, another requirement might be that the response be close to critically damped so as to limit overshoot and oscillatory response after a disturbance. The simplified relationship expression for the damping ratio, therefore, highlights that the virtual inertia must be chosen to obtain the damping ratio thus limiting its choice. It can also be seen that, the role of virtual impedance is largely to affect the angle and potential to power gains. Again the simplified expression for damping ratio highlights that for a fixed damping ratio and droop, virtual inertia could be increased if the angle to real power gain is reduced, which could be achieved by an increase in virtual inductance. The increase in virtual inductance can also help decouple the effect of an active power reference change on reactive power output, i.e. reduce $H_{\mathrm{d}Q/\mathrm{d}\delta}$ (see Fig. 8*b*).

As regards reactive power, the reactive power droop gain, $K_q$ can be chosen larger in order to decouple the reactive power from active power, although on the other hand, this increases overshoot so that there is clearly a trade-off involved.

## 5 Hardware validation

To further validate the above analysis and also to provide an example, results from a small-scaled hardware experiment are presented. The design requirements are reference voltage $V^* = 100\,\mathrm{V}$, reference frequency $\omega^* = 100\pi$ rad/s, the converter capacity $S = 800\mathrm{VA}$, the DC source power $P_{\mathrm{DC}} = 300\,\mathrm{W}$, the storage rate of discharge $P_s = 250\,\mathrm{W}$, the settling time $t_s < 2\,\mathrm{s}$, and the line impedance $R_g + 2\pi f_g L_g = 1.44 + 100\pi \times 0.033\,\Omega$.

Designing for a grid frequency deviation, $\Delta f = 0.1\,\mathrm{Hz}$, substituting into (42) gives the droop/damping gain $K_d$:

$$K_d = \frac{P_s}{2\pi\Delta f} = \frac{300}{2\pi \times 0.1} = 400\,\mathrm{W/Hz} \tag{42}$$

The initial grid voltage $U_g = 100\,\mathrm{V}$ and frequency $\omega_g = 100\pi$ rad/s and we assume that the initial electric potential $E_0 = 100\,\mathrm{V}$, and there is no virtual impedance. Then, according to (37), the initial angle difference $\delta_0$ can be calculated

$$\delta_0 = \sin^{-1}\frac{(P_{\mathrm{DC}} + P_S)2\pi f_g L_g}{E_0 U_g} = 0.6739\,\mathrm{rad}$$

For illustration purposes, we consider two values of virtual impedance, $2\pi f_g L_v = 100\pi \times 0.011\,\Omega$, and $2\pi f_g L_v = 100\pi \times 0.011\,\Omega$ which decreases and increases the actual line inductance by 33.3%, respectively. Substituting these values of virtual impedance and $\delta_0 = 0.6739$ into (20), (21), (24) and (25) gives: when the virtual impedance is negative, $H_{\mathrm{d}P/\mathrm{d}\delta} = 1867$ and when the virtual impedance is positive, $H_{\mathrm{d}P/\mathrm{d}\delta} = 902$.The damping ratio $\xi$ is given by:

$$\xi = \frac{K_d}{2\sqrt{JH_{\mathrm{d}P/\mathrm{d}\delta}}} = \frac{400}{2\sqrt{JH_{\mathrm{d}P/\mathrm{d}\delta}}}$$

and we present both underdamped case with $J = 20$ and $\xi \in [1.04,\ 1.49]$, and overdamped case with $J = 80$ and $\xi \in [0.52,\ 0.74]$.

The reactive power droop gain $K_q$ considering its constraint is given by

$$K_q < \frac{U_{\max} - U_{\min}}{P_{\max} - P_{\min}} = \frac{(110 - 90)}{650} = 0.031$$

and the experiment tests values of $K_q = 0.01$ and $K_q = 0.03$ conditions.

The design of the VSC follows the design approach for a *dq*-frame voltage controlled VSC as given in [44], with controller settings as given in Table 1.

For the tests, the VSG experiences a reference active power step change from 0 to 300 W at 1 s, and a grid frequency ramp change from 50 to 49.9 Hz with 1 Hz/s slope at 4 s. The designed VSGs has been validated on the hardware in the loop OPAL-RT platform. The VSG transient response, i.e. the steady-state value, overshoot and settling time is predicted from the mathematical computation in Tables 2 and 3 with the above settings are given in Table 6. Fig. 12 depicts the measured output power results from the hardware tests.

In comparison with the hardware result, the predicted steady-state values, settling times and overshoot are accurate. Furthermore, these results follow the analysis from Section 4.1.2. For example, reducing the virtual inductance can reduce the settling time (compare C1 and C3, C2 and C4). When the other settings are identical, the overdamped situation with smaller inertia settles faster than the underdamped situation (compare C1 and C2, C3 and C4). Moreover, the reactive droop gain has no effect on settling time (compare C4 and C5).

From Fig. 12*a*, as expected, in the underdamped situation with inertia $J = 80$, reducing the virtual inductance results in an increase in overshoot.

Under the active power variation, the reactive power output Fig. 12*b* illustrates the degree of coupling. Since the reference reactive power is zero, the curves which are closest to the zero value represent the lower degree of coupling. The results serve to validate the analysis that increasing the virtual inductance or increasing the reactive power droop gain helps to decouple the reactive power output from active power operation.

**Table 6** VSG Transient Response Prediction

| transfer function | C1:$L_V$ = - 0.011$J$ = 20$K_q$ = 0.01 | C2:$L_V$ = − 0.011$J$ = 80$K_q$ = 0.01 | C3:$L_V$ = 0.011$J$ = 20$K_q$ = 0.01 | C4:$L_V$ = 0.011$J$ = 80$K_q$ = 0.01 | C5:$L_V$ = 0.011$J$ = 80$K_q$ = 0.03 |
|---|---|---|---|---|---|
| damping ratio | 1.01 | 0.492 | 1.366 | 0.683 | 0.683 |
| steady-state at 3 s | $P$ = 300$Q$ = −20 | $P$ = 300$Q$ = −20 | $P$ = 300 $Q$ = −11 | $P$ = 300$Q$ = −11 | $P$ = 300$Q$ = −9 |
| steady-state at 6 s | $P$ = 551$Q$ = 19 | $P$ = 551$Q$ = 19 | $P$ = 551 $Q$ = 11 | $P$ = 551$Q$ = 11 | $P$ = 551$Q$ = 9 |
| overshoot at 1 s | — | $P$ = 351$Q$ = −36 | — | $P$ = 316$Q$ = −16 | $P$ = 315$Q$ = −15 |
| overshoot at 4 s | — | $P$ = 625$Q$ = 43 | — | $P$ = 565$Q$ = 14 | $P$ = 565$Q$ = 13 |
| settling time | 0.55 | 1.62 | 1.3 | 1.69 | 1.69 |

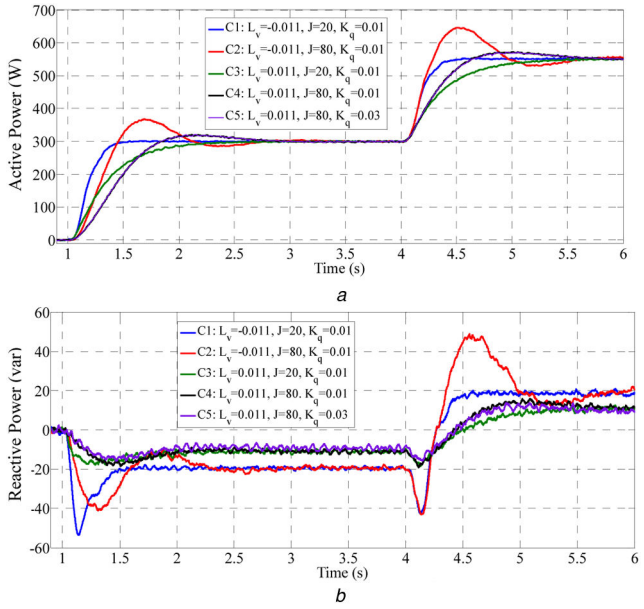


**Fig. 12** *Hardware experiment result for designed VSG*
***(a)*** Active power output, ***(b)*** Reactive power output

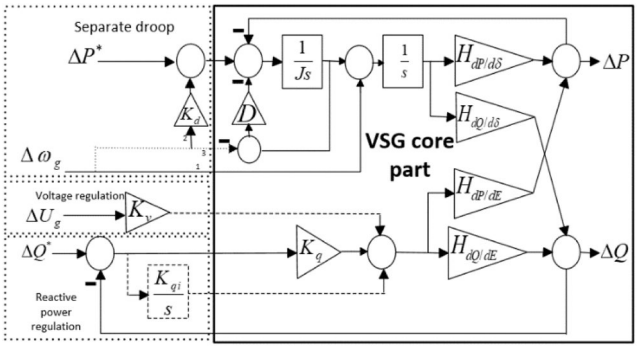


**Fig. 13** *Different VSG implementation methods*

## 6 Discussions

The analysis in the paper is applied to the VSG scheme where droop and damping are combined in a single parameter with equivalent droop and damping [7–12, 19, 20, 22, 27, 28, 34, 39, 40], and simple reactive power to voltage droop control [13–16, 23, 28, 37]. The analysis can, however, be extended to other schemes such as the use of separate droop and damping parameters [13–18, 21, 23, 32, 33, 37] or other reactive power regulation approaches such as voltage regulation [17, 18, 21, 22, 28] or reactive power control [19, 20]. The diagram in Fig. 13 indicates how such schemes could be added to the scheme analysed in the paper. For the scheme using separate droop and damping the droop contribution could be added as an outer loop which adjusts the power setpoint according to the deviation in frequency, measured by a PLL with transfer function $H(s)$. The transfer function from power reference changes to output power, $G_{P\_P}, G_{P\_Q}, G_{Q\_Q}, G_{Q\_P}$ remain identical to those derived above. However, the transfer function from grid frequency changes to output power becomes more complex in this case. Specifically, there now exists three components to this transfer function. One component is the same $G_{P\_\omega}$ transfer function as derived in this paper, the second is associated with the power setpoint change from the droop which is given by $K_dH(s)G_{P\_P}$, and the third is associated with the separate damping term, a full discussion of which is beyond the scope of this paper.

As regards the other reactive power controls these can be easily accommodated by the modification of the outer loop associated with determining $E$. These additions required to accommodate these different schemes are indicated by the blocks enclosed within the sections marked by broken lines in Fig. 13.

## 7 Conclusions

The paper introduced the large signal model for VSG control of a voltage controlled converter, and based on this develops a complete set of transfer functions which can be used to analyse the output real and reactive powers in response to changes in real and reactive powers references and grid frequency disturbances. Using these transfer functions the effect of various VSG design parameters such as inertia, droop/damping and virtual inertia on the VSG performance has been analysed. Moreover, the transfer functions can provide the basis for VSG controller design taking into account transient and steady-state performance and cross-coupling effects between real and reactive powers. The choice of droop gain and virtual inertia are clearly be linked through the requirement to satisfy transient performance criteria such as damping, overshoot and setting time. The inclusion of virtual impedance does give another degree of freedom in the choice of these parameters. Although the analysis in the paper is based on the VSG scheme with equivalent droop and damping, and simple reactive power to voltage droop control, it is possible to adapt to the analysis to schemes with separate droop and damping settings, or with other reactive power regulations.

## 8 Acknowledgments

This work was part of the Energy Systems Integration Partnership Programme (ESIPP) Project funded by the Science Foundation Ireland (SFI) Strategic Partnership Programme grant no. SFI/15/SPP/E3125.

## 9 References

[1] Beck, H., Hesse, R.: 'Virtual synchronous machine'. 2007 9th Int. Conf. on Electrical Power Quality and Utilisation, Barcelona, Spain, October 2007, pp. 1–6

[2] Van Wesenbeeck, M.P.N., De Haan, S.W.H., Varela, P., *et al.*: 'Grid tied converter with virtual kinetic storage'. 2009 IEEE Bucharest PowerTech, Bucharest, Romania, June/July 2009, pp. 1–7

[3] D'Arco, S., Suul, J.A.: 'Virtual synchronous machines – classification of implementations and analysis of equivalence to droop controllers for microgrids'. 2013 IEEE Grenoble PowerTech, Grenoble, France, June 2013, pp. 1–7

[4] Torres, L. M.A., Lopes, L.A.C., Morán, T. L.A., *et al.*: 'Self-tuning virtual synchronous machine: a control strategy for energy storage systems to support dynamic frequency control', *IEEE Trans. Energy Convers.*, 2014, **29**, (4), pp. 833–840

[5] Tamrakar, U., Galipeau, D., Tonkoski, R., *et al.*: 'Improving transient stability of photovoltaic-hydro microgrids using virtual synchronous machines'. IEEE Eindhoven PowerTech, Eindhoven, Netherlands, June/July 2015, pp. 1–6

[6] D'Arco, S., Suul, J.A.: 'Equivalence of virtual synchronous machines and frequency-droops for converter-based MicroGrids', *IEEE Trans. Smart Grid*, 2014, **5**, (1), pp. 394–395

[7] Zhang, L., Harnefors, L., Nee, H.: 'Power-synchronization control of grid-connected voltage-source converters', *IEEE Trans. Power Syst.*, 2010, **25**, (2), pp. 809–820

[8] Zhong, Q., Weiss, G.: 'Synchronverter: inverters that mimic synchronous generators', *IEEE Trans. Ind. Electron.*, 2011, **58**, (4), pp. 1259–1267

[9] Zhong, Q., Nguyen, P., Ma, Z., *et al.*: 'Self-synchronized synchronverters: inverters without a dedicated synchronization unit', *IEEE Trans. Power Electron.*, 2014, **29**, (2), pp. 617–630

[10] Zhong, Q.: 'Virtual synchronous machines: a unified interface for grid integration', *IEEE Power Electron. Mag.*, 2016, **3**, (4), pp. 18–27

[11] Zhong, Q., Ma, Z., Ming, W., *et al.*: 'Grid-friendly wind power systems based on the synchronverter technology', *Energy Convers. Manage.*, 2015, **89**, (1), pp. 719–726

[12] Ming, W., Zhong, Q.: 'Synchronverter-based transformerless PV inverters'. IECON 2014–40th Annual Conf. of the IEEE Industrial Electronics Society, Dallas, TX, USA, November 2014, pp. 4396–4401

[13] D'Arco, S., Suul, J.A., Fosso, O.B.: 'A virtual synchronous machine implementation for distributed control of power converters in smart grids', *Electr. Power Syst. Res.*, 2015, **122**, pp. 180–197

[14] D'Arco, S., Suul, J.A., Fosso, O.B.: 'Small-signal modelling and parametric sensitivity of a virtual synchronous machine'. 2014 Power Systems Computation Conf., Wroclaw, Poland, August 2014, pp. 1–9

[15] D'Arco, S., Suul, J.A., Fosso, O.B.: 'Control system tuning and stability analysis of virtual synchronous machines'. 2013 Energy Conversion Congress and Exposition, Denver, CO, USA, September 2013, pp. 2664–2671

[16] Mo, O., D'Arco, S., Suul, J.A.: 'Evaluation of virtual synchronous machines with dynamic or quasi-stationary machine models', *IEEE Trans. Ind. Electron.*, 2017, **64**, (7), pp. 5952–5962

[17] Liu, J., Miura, Y., Bevrani, H., *et al.*: 'Enhanced virtual synchronous generator control for parallel inverters in microgrids', *IEEE Trans. Smart Grid*, 2017, **8**, (5), pp. 2268–2277

[18] Alipoor, J., Miura, Y., Ise, T.: 'Stability assessment and optimization methods for microgrid with multiple VSG units', *IEEE Trans. Smart Grid*, 2018, **9**, (2), pp. 1462–1471

[19] Shi, K., Ye, H., Song, W., *et al.*: 'Virtual inertia control strategy in microgrid based on virtual synchronous generator technology', *IEEE. Access.*, 2018, **6**, pp. 27949–27957

[20] Shi, K., Song, W., Xu, P., *et al.*: 'Low-voltage ride-through control strategy for a virtual synchronous generator based on smooth switching', *IEEE. Access.*, 2018, **6**, pp. 2703–2711

[21] Ma, Y., Cao, W., Yang, L., *et al.*: 'Virtual synchronous generator control of full converter wind turbines with short-term energy storage', *IEEE Trans. Ind. Electron.*, 2017, **64**, (11), pp. 8821–8831

[22] Chen, J., Liu, L., Milano, F., *et al.*: 'Placement of virtual synchronous generator controlled electric storage combined with renewable generation'. PowerTech, Milano, Italy, 23–27 June 2019

[23] Suul, J.A., D'Arco, S., Guidi, G.: 'Virtual synchronous machine-based control of a single-phase bi-directional battery charger for providing vehicle-to-grid services', *IEEE Trans. Ind. Appl.*, 2016, **52**, (4), pp. 3234–3244

[24] Chen, D., Xu, Y., Huang, A.Q.: 'Integration of DC microgrids as virtual synchronous machines into the AC grid', *IEEE Trans. Ind. Electron.*, 2017, **64**, (9), pp. 7455–7466

[25] Kerdphol, T., Rahman, F.S., Watanabe, M., *et al.*: 'Enhanced virtual inertia control based on derivative technique to emulate simultaneous inertia and damping properties for microgrid frequency regulation', *IEEE Access.*, 2019, **7**, pp. 14422–14433

[26] Kerdphol, T., Rahman, F.S., Mitani, Y., *et al.*: 'Robust virtual inertia control of an islanded microgrid considering high penetration of renewable energy', *IEEE. Access.*, 2018, **6**, pp. 625–636

[27] Chen, J., Liu, M., O'Donnell, T.: 'Replacement of synchronous generator by virtual synchronous generator in the conventional power system'. 2019 IEEE PES General Meeting, Atlanta, GA, USA, August 2019, pp. 1–5

[28] Chen, J., Liu, M., O'Loughlin, C., *et al.*: 'Modelling, simulation and hardware-in-the-loop validation of virtual synchronous generator control in low inertia power system'. 2018 Power Systems Computation Conf. (PSCC), Dublin, Ireland, June 2018, pp. 1–7

[29] Cvetkovic, I., Boroyevich, D., Burgos, R., *et al.*: 'Modeling of a virtual synchronous machine-based grid-interface converter for renewable energy systems integration'. 2014 IEEE 15th Workshop on Control and Modeling for Power Electronics (COMPEL), Santander, Spain, June 2014, pp. 1–7

[30] Cao, Y., Wang, W., Tan, Y., *et al.*: 'A virtual synchronous generator control strategy for VSC-MTDC systems', *IEEE Trans. Energy Convers.*, 2018, **33**, (2), pp. 750–761

[31] Fang, J., Li, H., Tang, Y., *et al.*: 'Distributed power system virtual inertia implemented by grid-connected power converters', *IEEE Trans. Power Electron.*, 2018, **33**, (10), pp. 8488–8499

[32] Alipoor, J., Miura, Y., Ise, T.: 'Power system stabilization using virtual synchronous generator with alternating moment of inertia', *IEEE J. Emerging Sel. Topics Power Electron.*, 2015, **3**, (2), pp. 451–458

[33] Li, D., Zhu, Q., Lin, S., *et al.*: 'A self-adaptive inertia and damping combination control of VSG to support frequency stability', *IEEE Trans. Energy Convers.*, 2017, **32**, (1), pp. 397–398

[34] Shuai, Z., Hu, Y., Peng, Y., *et al.*: 'Dynamic stability analysis of synchronverter-dominated microgrid based on bifurcation theory', *IEEE Trans. Ind. Electron.*, 2017, **64**, (9), pp. 7467–7477

[35] Fang, J., Lin, P., Li, H., *et al.*: 'An improved virtual inertia control for three-phase voltage source converters connected to a weak grid', *IEEE Trans. Power Electron.*, 2019, **34**, (9), 8660–8670

[36] Li, G., Ma, F., Luo, A., *et al.*: 'Virtual impedance-based virtual synchronous generator control for grid-connected inverter under the weak grid situations', *IET Power Electron.*, 2018, **11**, (13), pp. 2125–2132

[37] Du, Y., Guerrero, J.M., Chang, L., *et al.*: 'Modeling, analysis, and design of a frequency-droop-based virtual synchronous generator for microgrid applications'. 2013 IEEE ECCE Asia Downunder, Melbourne, VIC, Australia, June 2013, pp. 643–649

[38] Wang, Z., Yi, H., Wu, J., *et al.*: 'Dynamic performance analysis of paralleled virtual synchronous generators under grid-connected and islanded mode'. 2017 IEEE Applied Power Electronics Conf. and Exposition (APEC), Tampa, FL, USA, March 2017, pp. 1326–1332

[39] Chen, J., O'Donnell, T.: 'Parameter constraints for virtual synchronous generator considering stability', *IEEE Trans. Power Syst.*, 2019, **34**, (3), pp. 2479–2481

[40] Wang, J., Wang, Y., Gu, Y., *et al.*: 'Synchronous frequency resonance of virtual synchronous generators and damping control'. 2015 9th Int. Conf. on Power Electronics and ECCE Asia (CPE-ECCE Asia), Seoul, South Korea, June 2015, pp. 1011–1016

[41] Pogaku, N., Prodanovic, M., Green, T.C.: 'Modeling, analysis and testing of autonomous operation of an inverter-based microgrid', *IEEE Trans. Power Electron.*, 2007, **22**, (2), pp. 613–625

[42] Zeng, Z., Zhao, R., Yang, H., *et al.*: 'Single-phase virtual synchronous generator for distributed energy sources'. 2013 Int. Conf. on Electrical Machines and Systems, Busan, South Korea, October 2013, pp. 190–195

[43] Kundur, P.: '*Power system stability and control*' (McGraw-Hill Education, NewYork, USA, 1994)

[44] Yazdani, A., Iravani, R.: '*Voltage-sourced converters in power system*' (Wiley IEEE Press, Canada, 2010)


## 10 Appendix

The appendix will give a detailed computation for the overshoot $G_{P\_\omega}$ and $G_{Q\_\omega}$.

Defining $c_1 = H_{\mathrm{d}P/\mathrm{d}\delta} - H_{\mathrm{d}Q/\mathrm{d}\delta}H_{\mathrm{d}P/\mathrm{d}E}\,(K_q/(1 + K_qH_{\mathrm{d}Q/\mathrm{d}E}))$

$$\begin{aligned} G_{P\_\omega} &= \frac{\left(H_{\mathrm{d}P/\mathrm{d}\delta} - H_{\mathrm{d}Q/\mathrm{d}\delta}H_{\mathrm{d}P/\mathrm{d}E}\dfrac{K_q}{1 + K_qH_{\mathrm{d}Q/\mathrm{d}E}}\right)(Js + K_d)}{Js^2 + K_ds + H_{\mathrm{d}P/\mathrm{d}\delta} - H_{\mathrm{d}Q/\mathrm{d}\delta}H_{\mathrm{d}P/\mathrm{d}E}(K_q/(1 + K_qH_{\mathrm{d}Q/\mathrm{d}E})} \\ &= c_1\frac{s + (K_d/J)}{s^3 + (K_d/J)s^2 + (c_1/J)s} \\ &= c_1\frac{s}{s^3 + (K_d/J)s^2 + (c_1/J)s} + c_1\frac{K_d/J}{s^3 + (K_d/J)s^2 + (c_1/J)s} \end{aligned} \tag{43}$$

Defining $\omega_{P\_\omega} = \sqrt{(c_1/J) - (K_d^2/4J^2)}$ and $a_{P\_\omega} = K_d/2J$, and computing each part in (43) separately:

$$\begin{aligned} c_1\frac{s}{s^3 + (K_d/J)s^2 + (c_1/J)s} &= c_1\frac{\omega_{P\_\omega}}{(s + a_{P\_\omega})^2 + \omega_{P\_\omega}^2}\cdot\frac{1}{\omega_{P_f}} \\ &= \frac{c_1}{\omega_{P\_\omega}}\mathrm{e}^{-a_{P\_f}\cdot t}\sin(\omega_{P\_\omega}\cdot t) \end{aligned} \tag{44}$$

(see (45))

Inverse Laplace transform on (43):

$$c(t) = K_d - \mathrm{e}^{-a_{P\_\omega}\cdot t}K_\alpha\sin(\omega_{P\_\omega}\cdot t + \alpha) \tag{46}$$

$$\begin{aligned} c_1\frac{K_d/J}{s^3 + (K_d/J)s^2 + (c_1/J)s} &= K_d\left(\frac{1}{s} - \frac{s + (K_d/J)}{s^2 + (K_d/J)s + (c_1/J)}\right) \\ &= K_d\left(\frac{1}{s} - \frac{s + a_{P\_\omega}}{(s + a_{P\_\omega})^2 + \omega_{P\_\omega}^2} - \frac{a_{P\_\omega}}{(s + a_{P\_\omega})^2 + \omega_{P\_\omega}^2}\right) \\ &= K_d\left(1 - \mathrm{e}^{-a_{P\_\omega}\cdot t}\cos(\omega_{P\_\omega}\cdot t) - \frac{a_{P\_f}}{\omega_{P_f}}\mathrm{e}^{-a_{P\_\omega}\cdot t}\sin(\omega_{P\_\omega}\cdot t)\right) \end{aligned} \tag{45}$$

$$\begin{aligned}\frac{\mathrm{d}c(t)}{\mathrm{d}t} &= a_{P\_\omega}\mathrm{e}^{-a_{P\_\omega}\cdot t}K_\alpha\sin\left(\omega_{P_f}\cdot t+\alpha\right)\\ &\quad -\omega_{P\_\omega}\mathrm{e}^{-a_{P\_\omega}\cdot t}K_\alpha\cos(\omega_{P\_\omega}\cdot t+\alpha)\\ &= \mathrm{e}^{-a_{P\_\omega}\cdot t}K_\alpha K_\beta\sin(\omega_{P\_\omega}\cdot t+\alpha-\beta)\end{aligned} \tag{47}$$

When (47) equals to 0 could compute the time for overshoot (raising time):

$$t_{p\_\omega} = \frac{\tan^{-1}(\omega_{P\_\omega}/a_{P\_\omega}) - \tan^{-1}(K_d\omega_{P\_\omega}/(K_d a_{P\_\omega} - c_1))}{\omega_{P\_\omega}} \tag{48}$$

Then overshoot is:

(see (49))

Similarly, it could obtain $OP_{Q\_f}$ by defining $c_2 = H_{\mathrm{d}Q/\mathrm{d}\delta}/(1+K_qH_{\mathrm{d}Q/\mathrm{d}E})$, $c_3 = -K_qH_{\mathrm{d}P/\mathrm{d}E}((1+K_qH_{\mathrm{d}Q/\mathrm{d}E})/H_{\mathrm{d}Q/\mathrm{d}\delta}) + H_{\mathrm{d}P/\mathrm{d}\delta}$, $a_{Q\_\omega} = K_d/2J$, $\omega_{Q\_\omega} = \sqrt{(c_3/J) - (K_d^2/4J^2)}$.

$$\begin{aligned}G_{Q\_\omega} &= \frac{(H_{\mathrm{d}Q/\mathrm{d}\delta}/(1+K_qH_{\mathrm{d}Q/\mathrm{d}E}))(Js+K_d)}{Js^2+K_ds-K_qH_{\mathrm{d}P/\mathrm{d}E}((1+K_qH_{\mathrm{d}Q/\mathrm{d}E})/H_{\mathrm{d}Q/\mathrm{d}\delta})+H_{\mathrm{d}P/\mathrm{d}}}\\ &= c_2\frac{s+(K_d/J)}{s^3+(K_d/J)s^2+(c_3/J)s}\\ &= c_2\frac{s}{s^3+(K_d/J)s^2+(c_3/J)s}+c_2\frac{K_d/J}{s^3+(K_d/J)s^2+(c_3/J)s}\end{aligned} \tag{50}$$

$$c_2\frac{s}{s^3+(K_d/J)s^2+(c_3/J)s} = \frac{c_2}{\omega_{Q\_f}}\mathrm{e}^{-a_{Q\_\omega}\cdot t}\sin(\omega_{Q\_\omega}\cdot t) \tag{51}$$

(see (52))

$$c(t) = \frac{K_dc_2}{c_3} - c_2\mathrm{e}^{-a_{Q\_\omega}\cdot t}K_\alpha\sin(\omega_{Q\_\omega}\cdot t+\alpha) \tag{53}$$

$$\frac{\mathrm{d}c(t)}{\mathrm{d}t} = \mathrm{e}^{-a_{Q\_\omega}\cdot t}c_2K_\alpha K_\beta\sin(\omega_{Q\_\omega}\cdot t+\alpha-\beta) \tag{54}$$

$$\begin{aligned}t_{Q\_\omega} &= \frac{1}{\omega_{Q\_\omega}}\Bigg(\tan^{-1}(\omega_{Q\_\omega}/a_{Q\_\omega})\\ &\quad -\tan^{-1}\frac{K_d/c_3}{(K_da_{Q\_\omega}/c_3\omega_{Q\_\omega})-(1/\omega_{Q\_\omega})}\Bigg)\end{aligned} \tag{55}$$

$$\begin{aligned}\mathrm{d}P_{Q\_\omega} &= \frac{c_2}{\omega_{Q\_f}}\mathrm{e}^{-a_{Q\_\omega}\cdot t}\sin(\omega_{Q\_\omega}\cdot t)\\ &\quad +\frac{K_dc_2}{c_3}\left(1-\mathrm{e}^{-a_{Q\_\omega}\cdot t}\cos(\omega_{Q\_\omega}\cdot t)-\frac{a_{Q\_\omega}}{\omega_{Q\_\omega}}\mathrm{e}^{-a_{Q\_\omega}\cdot t}\sin(\omega_{Q\_\alpha}\right.\end{aligned} \tag{56}$$

$$\begin{aligned}OP_{P\_\omega} &= \frac{c_1}{\omega_{P\_\omega}}\mathrm{e}^{-a_{P\_\omega}\cdot t}\sin(\omega_{P\_\omega}\cdot t_{P\_\omega})\\ &\quad +K_d\left(1-\mathrm{e}^{-a_{P\_\omega}\cdot t}\cos(\omega_{P\_\omega}\cdot t_{P\_\omega})-\frac{a_{P\_\omega}}{\omega_{P\_\omega}}\mathrm{e}^{-a_{P\_\omega}\cdot t}\sin(\omega_{P\_\omega}\cdot t_{P\_\omega})\right)\end{aligned} \tag{49}$$

$$\begin{aligned}&c_2\frac{K_d/J}{s^3+(K_d/J)s^2+(c_3/J)s}\\ &\quad = \frac{K_dc_2}{c_3}\left(1-\mathrm{e}^{-a_{Q\_\omega}\cdot t}\cos(\omega_{Q\_\omega}\cdot t)-\frac{a_{Q\_\omega}}{\omega_{Q\_\omega}}\mathrm{e}^{-a_{Q\_\omega}\cdot t}\sin(\omega_{Q\_\omega}\cdot t)\right)\end{aligned} \tag{52}$$